Structure of the electron diffusion region in magnetic reconnection with small guide fields

by

Jonathan Ng

Submitted to the Department of Physics
in partial fulfillment of the requirements for the degree of

Bachelor of Science in Physics

at the

MASSACHUSETTS INSTITUTE OF TECHNOLOGY

June 2012

Author .....
Department of Physics
May 11, 2012

Certified by .....
Jan Egedal-Pedersen
Associate Professor of Physics
Thesis Supervisor

Accepted by .....
Nergis Mavalvala
Senior Thesis Coordinator, Department of Physics

Structure of the electron diffusion region in magnetic reconnection with small guide fields

by

Jonathan Ng

Submitted to the Department of Physics
on May 11, 2012, in partial fulfillment of the
requirements for the degree of
Bachelor of Science in Physics

Abstract

Observations in the Earth's magnetotail and kinetic simulations of magnetic reconnection have shown high electron pressure anisotropy in the inflow of electron diffusion regions. This anisotropy has been accurately accounted for in a new fluid closure for collisionless reconnection. By tracing electron orbits in the fields taken from particle-in-cell simulations, the electron distribution function in the diffusion region is reconstructed at enhanced resolutions. For antiparallel reconnection, this reveals its highly structured nature, with striations corresponding to the number of times an electron has been reflected within the region, and exposes the origin of gradients in the electron pressure tensor important for momentum balance. The addition of a guide field changes the nature of the electron distributions, and the differences are accounted for by studying the motion of single particles in the field geometry. Finally, the geometry of small guide field reconnection is shown to be highly sensitive to the mass ratio.

Thesis Supervisor: Jan Egedal-Pedersen
Title: Associate Professor of Physics

Acknowledgments

The completion of this thesis would not have been possible without the assistance of the following people. First, I would like to thank Prof. Jan Egedal, for getting me started on this project, introducing me to this field of physics and providing invaluable advice throughout the entire process. Also, for obtaining enough computers so I could get simulations done on a timely basis.

Dr. William Daughton, for providing all the terabytes[1] of simulation data used in this thesis, without whom this project might not have existed.

Dr.[2] Ari Lê, whose work on the equations of state led directly to this project, and for advice and for attempting to procure a copy of the Times[3].

The process of writing the thesis would have been a lot more stressful without the rest of the Versatile Toroidal Facility (VTF) group[4], Arturs Vrublevskis, Obioma Ohia, Peter Montag, Samuel Schaub and Alya AlQaydi.

Phil, for use of his Remington, which was an extremely effective instrument of destruction and stress relief[5].

Three setters[6]: one spider-related, a very distinguished tree, and a light breeze. (7, 9, 5)[7]

A well-known author whose name I shall not mention, for inspiring me to write lots of footnotes[8].

So long, and thanks for all the fish![9]

[1] On the order or ten to a hundred. Perhaps petabytes will be reached after I leave.

[2] Since I wrote this after May 4, 2012

[3] Sadly the attempt failed, but it was valiant nonetheless.

[4] If that's what we're calling ourselves these days.

[5] There is something therapeutic about breaking stuff into millions of minuscule pieces. I should also thank the Remington for shooting nicely.

[6] There are others of course, but these stand out.

[7] Solutions available with the next edition. I now have a much greater appreciation for partners, points, rivers, royalty, sailors and many other things.

[8] Unfortunately I was not able to make the footnotes longer than the text, as is his wont. In addition, I do not believe I have any footnotes in the thesis proper.

[9] Adams, 1984

Structure of the electron diffusion region in magnetic reconnection with small guide fields

by

Jonathan Ng

Submitted to the Department of Physics
in partial fulfillment of the requirements for the degree of

Bachelor of Science in Physics

at the

MASSACHUSETTS INSTITUTE OF TECHNOLOGY

June 2012

Author .....
Department of Physics
May 11, 2012

Certified by .....
Jan Egedal-Pedersen
Associate Professor of Physics
Thesis Supervisor

Accepted by .....
Nergis Mavalvala
Senior Thesis Coordinator, Department of Physics

Contents

List of Figures

Chapter 1

Introduction

1.1 Brief overview of Plasma Physics

1.1.1 Definition of a plasma

According to the textbook by Chen [1],

> *A plasma is a quasineutral gas of charged and neutral particles which exhibits collective behaviour.*

Quasineutrality implies that the number density of positive and negative charges is approximately equal, while collective behaviour differentiates a plasma from an ordinary ionised gas.

For a more rigorous definition, there are three standard criteria which must be fulfilled for a gas to be defined as a plasma. The first pertains to the shielding of DC electric fields by the plasma, which is measured by the Debye length λ_D [2] where

$$\frac{1}{\lambda_D^2} = \frac{1}{\lambda_{De}^2} + \frac{1}{\lambda_{Di}^2} = \frac{e^2 n_0}{\epsilon_0 T_e} + \frac{e^2 n_0}{\epsilon_0 T_i}. \tag{1.1}$$

Here n_0 is the background plasma density, e is the electric charge, ϵ_0 is the permittivity of free space and T_i, T_e are the ion and electron temperatures, where the Boltzmann constant has been absorbed. The Debye length is a measure of the length scale over which the DC field is shielded, and for a gas to be a plasma, its dimensions must be

much larger than the Debye length or $L \gg \lambda_D$ [1, 2]. This shielding effect also gives rise to quasineutrality as mentioned earlier.

The second criterion involves the shielding of AC fields, and involves the electron plasma frequency $\omega_{pe} = \sqrt{n_0 e^2/m_e \epsilon_0}$, which is the characteristic oscillation frequency of plasma oscillations (where all the electrons are displaced from the ion background) [1]. For a gas to be a plasma, characteristic frequencies must be much lower than the plasma frequency, or AC fields will not be effectively shielded [2].

The final criterion is necessary for collective behaviour, and requires that the long range interactions dominate collisional interactions. This is measured by the plasma parameter Λ_D, which is the number of particles in a sphere with radius λ_D, and must be much greater than one for collective effects to be important [1, 2].

1.1.2 Descriptions of plasmas

A full description of a (non-relativistic) plasma involves the coupled Maxwell-Boltzmann system of equations [1], also called kinetic theory, which requires solving the Boltzmann equation for the distribution function f_s of each plasma species

$$\frac{\partial f_s}{\partial t} + \mathbf{v} \cdot \nabla f_s + \frac{\mathbf{F}}{m} \cdot \frac{\partial f_s}{\partial \mathbf{v}} = \left(\frac{\partial f_s}{\partial t}\right)_{\text{coll}}. \tag{1.2}$$

The left hand side of the equation describes the streaming of particles in phase space, while the right hand side accounts for collisions. In the later chapters of this thesis, the collision term will be neglected and Eq. (1.2) will reduce to the Vlasov equation. The differential equations have seven independent variables and are coupled to Maxwell's equations through moments of f which give the charge density and current, making solving the entire system difficult.

As in fluid dynamics, the kinetic description can be approximated by taking velocity moments of the Boltzmann equation to obtain fluid equations. This gives rise to the two-fluid model of a plasma, with the ions and electrons considered as separate fluids. The derivation of a fluid model leads to more unknowns than equations, which gives rise to a closure problem which requires an additional equation based on phys-

ical principles. This will be described in more detail in Chapter 2, where a closure relevant to collisionless reconnection is derived.

Finally, the simplest description of a plasma is the Magnetohydrodynamic (MHD) approximation, a model which treats the plasma as a single fluid [1, 2]. This treatment of a plasma is less accurate than the previous models, but is easier to solve and is a good description of macroscopic behaviour.

There is much that has been passed over in this brief overview of plasma physics, and References [1, 2] may be useful for a more thorough treatment.

1.2 Magnetic Reconnection

Magnetic reconnection is a change in topology of the magnetic field lines in a plasma, in which the field lines are broken and reattached, often with a substantial conversion of stored magnetic energy to the kinetic energy of accelerated particles [3, 4, 5]. It is believed to play a vital role in a variety of laboratory and astrophysical plasma processes, including sawtooth crashes in tokamaks, solar flares, magnetic substorms in the Earth's magnetosphere and coronal mass ejections [4, 6].

The mechanism of reconnection was first proposed by Dungey in relation to solar flares [7], and this was soon followed by the development of the classic Sweet-Parker model, which uses the framework of resistive magnetohydrodynamics (MHD) [8]. More recent work has shown that two-fluid [9, 10] and kinetic [11] effects also play an important role in the reconnection process.

In order for reconnection to occur, the frozen in condition of ideal magnetohydrodynamics (MHD), $\mathbf{E} + \mathbf{v} \times \mathbf{B} = \mathbf{0}$ must be broken, so that field lines do not remain tied to the plasma. A key area of interest is thus the electron diffusion region, where the electron motion decouples from the magnetic field lines, which is necessary for reconnection to occur. This is described by the generalised Ohm's law, which can be obtained from electron momentum balance.

$$\mathbf{E} + \mathbf{v} \times \mathbf{B} = \eta \mathbf{J} + \frac{1}{ne}\mathbf{J} \times \mathbf{B} - \frac{1}{ne}\nabla \cdot \mathbf{P} + \frac{m_e}{ne^2}\frac{\partial \mathbf{J}}{\partial t} \tag{1.3}$$

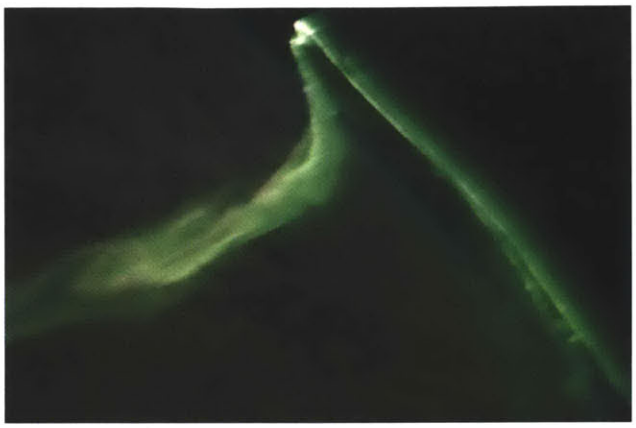

Figure 1-1: (colour) The Aurora Australis, caused by energetic charged particles produced by reconnection in the magnetotail interacting with the atmosphere. Source: NASA

On the right hand side of this equation, the first term describes the effect of resistivity, the second is the Hall term, the third is due to electron pressure and the final term is the effect of electron inertia. Understanding the role they play in the reconnection processes continues to be an important area of reconnection research [4].

In the following sections a brief review of reconnection models is presented.

1.3 Sweet-Parker Reconnection

The earliest model of reconnection was developed by Sweet and Parker in 1957 [8], using the framework of resistive MHD. The geometry of the model is shown in Fig. 1-2, with a current sheet of width d and length L between two oppositely directed magnetic fields.

Assuming steady state, and keeping only the resistive term in Equation (1.3), the generalised Ohm's law reduces to

$$\mathbf{E} + \mathbf{v} \times \mathbf{B} = \eta \mathbf{J}. \tag{1.4}$$

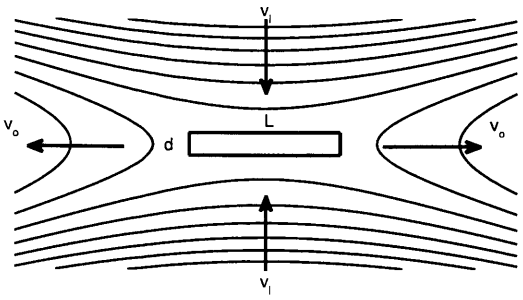

Figure 1-2: Sweet-Parker reconnection geometry.

This can be combined with Faraday's Law to obtain the induction equation

$$\frac{\partial \mathbf{B}}{\partial t} = \nabla \times (\mathbf{v} \times \mathbf{B}) + \frac{\eta}{\mu_0} \nabla^2 \mathbf{B}. \tag{1.5}$$

From the above equation, continuity and pressure balance, it can be shown that

$$\frac{v_I}{v_A} = \frac{d}{L} = \frac{1}{\sqrt{S}}, \tag{1.6}$$

where it has been assumed that the outflow speed is the Alfvén speed, and $S = \frac{\mu_0 V_A L}{\eta}$ is the Lundquist number, which is the ratio of the resistive diffusion time to the Alfvén wave crossing timescale [3, 4, 5]. The time scale for reconnection would then be $\tau \approx \sqrt{S}(L/v_A)$.

While Sweet-Parker reconnection has been observed experimentally in collisional plasmas [12], there are limitations to this model. The time scales involved are much too slow to explain fast reconnection. For example, in the solar corona, $S \approx 10^{12}$, $L/v_A \approx 10$s, giving $\tau \approx 10^7$s, which is much larger than the duration of a solar flare [4, 5]. Furthermore, the model fails to explain how reconnection takes place in collisionless plasmas, such as the magnetotail.

1.4 Fast Reconnection

1.4.1 Petschek Model

The discrepancy between the time scales of the Sweet-Parker model and solar flares led to the development of fast reconnection models, the earliest of which was the Petschek model, first proposed in 1964 [13]. While still working in the MHD picture, the model introduces slow switch-off shocks which widen the exhaust and allow the Sweet-Parker layer to be much shorter. After some analysis, a much faster reconnection rate is obtained [5, 13], with

$$v_I = \frac{\pi}{8 \ln S} V_A. \tag{1.7}$$

While the reconnection rates agree with experimental observations, in simulations with constant resistivity, the slow shocks have only been observed at length scales comparable to the Sweet-Parker length [4]. The associated slow shocks have also not been observed experimentally in the laboratory [5].

1.4.2 Hall Reconnection

A more recent development has been Hall Reconnection, a model in which the electron and ion motion decouple near the x-line at scales smaller than the ion inertial length $d_i = c/\omega_{pi}$ [9, 10]. In this model the reconnection outflow is driven by whistler waves or Kinetic Alfvén waves, which also gives rise to the widening of the exhaust [9]. In addition, the results of the GEM Challenge [14] have shown that in various codes, fast reconnection takes place with similar reconnection rates as long as the Hall effect is included.

As further evidence for the importance of Hall physics, the quadrupolar magnetic field structure characteristic of Hall reconnection has been observed in both space [15, 16] and laboratory plasmas [17]. However, it should be noted that the Hall model does not contain a dissipation mechanism necessary for breaking field lines [5], and does not explain fast reconnection in pair plasmas, where the Hall term is absent [9].

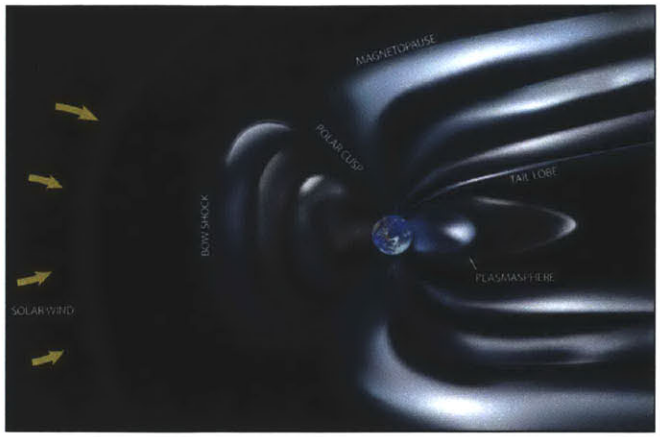

Figure 1-3: (colour) Cartoon of the Earth's magnetosphere. Source: NASA

For a more comprehensive review of reconnection models, the reader may peruse Refs. [3, 4, 18].

1.5 Relevance to the Magnetotail

Magnetic reconnection is one of the many plasma phenomena which takes place in the Earth's magnetotail. This is part of the magnetosphere, the region in space where the Earth's magnetic field dominates [3, 19], illustrated in Fig. 1-3. The structure of the magnetosphere is due to interactions between the solar wind and the Earth's magnetic field, and they are separated by a boundary known as the magnetopause, which is almost impermeable to plasma and magnetic fields [19].

The flow velocity of the solar wind is initially super Alfvénic, and it is slowed and heated at the bow shock, just upstream of the magnetopause [19]. Beyond this region, but before the magnetopause, lies the magnetosheath, in which the plasma flows around the magnetosphere and speeds up. On the nightside (away from the sun) of the Earth is the magnetotail, where magnetic field lines are stretched out in an elongated region.

In this almost collisionless environment, reconnection takes place on both the day-side and in the magnetotail, which allows field lines from the Earth to connect to those from the sun, and plasma from the solar wind to enter the earth's magnetosphere.

Reconnection in the magnetotail (and the rest of magnetosphere) has been the subject of *in situ* studies by numerous spacecraft, such as WIND [15], Cluster [16] and THEMIS [20], and the detailed study of the electron diffusion region, which is the subject of this thesis, will be one of the objectives of NASA's upcoming Magnetospheric Multiscale Mission (MMS) [21].

1.6 Outline

The remainder of this thesis is organised as follows. In Chapter 2, an overview of particle-in-cell (PIC) simulations is provided and the equations of state for collisionless reconnection [22] are reviewed. Chapters 3 and 4 are a detailed study of the electron diffusion region in simulations of reconnection with and without guide fields, and reveal the structure of the electron distribution in regions where the equations of state do not hold. Finally, the results of this work are summarised in Chapter 5.

Chapter 2

Equations of state for collisionless reconnection

2.1 Overview of kinetic simulations

Fully kinetic particle-in-cell (PIC) simulations are an important tool used to study the detailed physics of reconnection regions. These codes solve the Maxwell-Boltzmann system of equations by sampling the distribution function f with a large number of computational particles and evolving them in time within a spatial grid [23].

PIC simulations are computationally intensive, and are limited by the available resources. In particular, due to the necessity of resolving motion at the electron scale, the cost of an explicit PIC simulation scales with the mass ratio like $(m_i/m_e)^{(d+2)/2}$, where d is the number of spatial dimensions [23, 24]. As such, many simulations have been limited to two dimensions and artificially low mass ratios.

The data used in this thesis are the results of simulations using VPIC, a massively parallelised code which solves the relativistic Maxwell-Boltzmann system of equations. Details of the specific algorithms used can be found in [25]. The simulations used have 2 spatial and 3 velocity dimensions, and are translationally symmetric in the third spatial dimension. Magnetospheric coordinates are used [19], with the x axis along the outflow direction, z axis along the inflow, and y axis into the page. Open boundary conditions are used for both particles and fields [11].

In all the simulations studied, the initial state is a Harris sheet [26], with magnetic field profiles

$$B_x = B_0 \tanh(z/\Delta)$$
$$B_y = B_g$$
$$B_z = 0.$$

Here B_g is the guide field and is varied from 0 to $0.2B_0$. The Harris sheet is characterised by the following parameters: $T_i/T_e = 5$, $\omega_{\rm pe}/\omega_{\rm ce} = 2$, background density $= 0.23n_0$ and $v_{the}/c = 0.13$. Reconnection is initiated by a small initial perturbation and the systems are evolved in time.

2.2 Equations of state for collisionless reconnection

Recent observations in the Earth's magnetotail and kinetic simulations have revealed the existence of strong electron pressure anisotropy ($p_\parallel \gg p_\perp$) upstream of electron diffusion regions [22, 27, 28]. In particular, for antiparallel reconnection, simulations have shown that the diffusion region is characterised by a narrow layer containing electron jets. This is illustrated in Figs. 2-1(a) and (b), which show the pressure anisotropy and electron fluid velocity in the outflow direction.

In Figs. 2-1(c) and (d), gyrophase averaged electron distributions from the simulation inflow and the WIND spacecraft [29] are presented. The distributions are evidently anisotropic, and cannot be accounted for using standard fluid models.

Instead, the large pressure anisotropy and formation of elongated electron jets is explained by the guiding-centre trapping of electrons in a parallel potential [22, 30, 31]. Assuming the electron thermal speed is much larger than the Alfvén speed $v_{the} \gg v_A$ and the adiabatic invariance of the magnetic moment $\mu = mv_\perp^2/2B$, an expression for the distribution function can be determined.

Far upstream of reconnection regions in the ambient plasma, the distribution

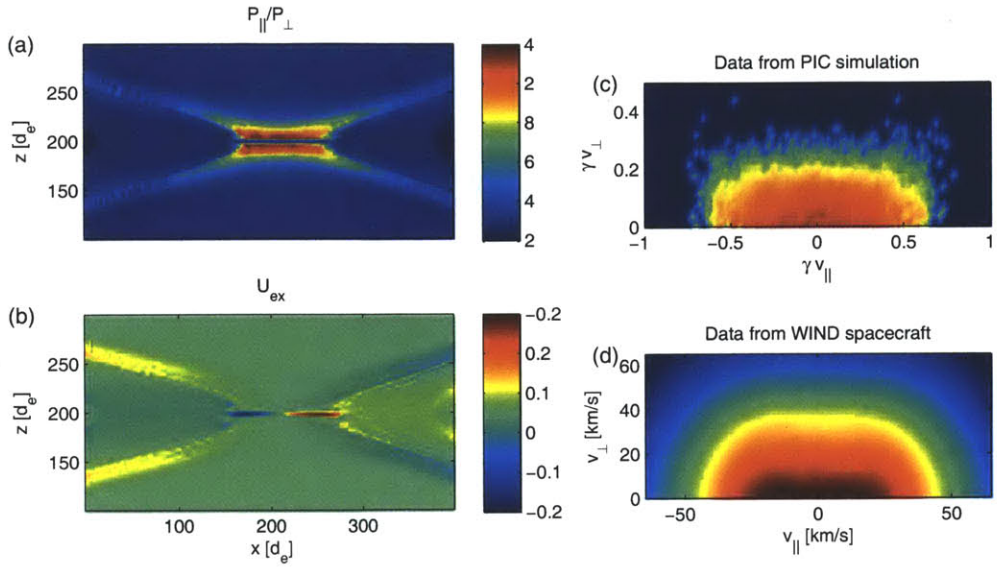

Figure 2-1: (colour) (a) Pressure anisotropy in a PIC simulation. (b) Elongated electron jets. (c) Particle data from the inflow of the simulation. (d) Electron data from the WIND spacecraft during a crossing of a reconnection region.

function f_∞ of the electrons is assumed to be an isotropic Maxwellian. Because of the conservation of the magnetic moment μ, the perpendicular velocity of electrons approaching the diffusion region decreases as B decreases. At the same time, electrons moving along a field line gain energy due to acceleration by parallel electric fields, so that the total energy of an electron can be written as $\mathcal{E} = \mathcal{E}_\infty + e\Phi_{||}$, where $\mathcal{E}_\infty$ is the initial energy and $\Phi_{||}$ is an acceleration potential defined by

$$\Phi_{||}(x) = \int_{\mathbf{x}}^{\infty} \mathbf{E} \cdot d\mathbf{l}, \tag{2.1}$$

where the integration is carried out along the magnetic field lines. Here it should be emphasised that $\Phi_{||}$ is a pseudo potential characterising the minimal energy required for an electron to escape the region in a straight shot along a field line. It should not be confused with the electrostatic potential, and can in fact take the opposite sign in certain regions [30, 32].

Using Liouville's theorem, which states that $df/dt = 0$ along particle trajectories, points in the reconnection region can be mapped to the ambient plasma, allowing

the distribution to be determined by $f(\mathbf{x}, \mathbf{v}) = f_\infty(\mathcal{E}_\infty)$. It is important to note that particles can be divided into two categories – trapped particles which have almost no initial parallel velocity and drift into the region, and passing particles, which reach the region in a single shot along a field line [30].

From the conservation arguments above, the energy of particles at infinity can expressed in terms of $\mathcal{E}, \mu$ and the ambient magnetic field B_∞

$$\mathcal{E}_\infty = \begin{cases} \mathcal{E} - e\Phi_\parallel, & \text{passing} \\ \mu B_\infty, & \text{trapped} \end{cases} \tag{2.2}$$

The distribution function thus takes the form

$$f(\mathbf{x}, \mathbf{v}) = \begin{cases} f_\infty\left(\mathcal{E} - e\Phi_\parallel\right), & \text{passing} \\ f_\infty\left(\mu B_\infty\right), & \text{trapped} \end{cases} \tag{2.3}$$

The form of this distribution is illustrated in Fig. 2-2, which displays the relevant parameters $\Phi_\parallel$ and B/B_∞, together with contours of f superimposed over the particle data taken directly from a kinetic simulation. As can be seen, there is good agreement between the model and the data.

As shown in Ref. [22], expressions of the density and parallel and perpendicular pressures as functions of $\Phi_\parallel$ and B are obtained by taking moments of the distribution function. By eliminating $\Phi_\parallel$, equations of state for the pressure $p_\parallel(n, B)$ and $p_\perp(n, B)$ can be found. The scalings $p_\parallel \propto n^3/B^2$ and $p_\perp \propto nB$ then explain the strong pressure anisotropy in regions of high density and small magnetic fields.

In reconnection with a guide field, good agreement has been found between the equations of state and kinetic simulations [22]. However, in antiparallel reconnection, where there is no guide field, the equations break down in a thin layer close to the x-line due to the electrons becoming unmagnetised and the magnetic moment no longer being conserved. This is shown in Fig. 2-3, in which the equations of state are compared to simulation data for antiparallel and guide field reconnection. Nevertheless, the strong anisotropy does explain the formation of elongated electron jets –

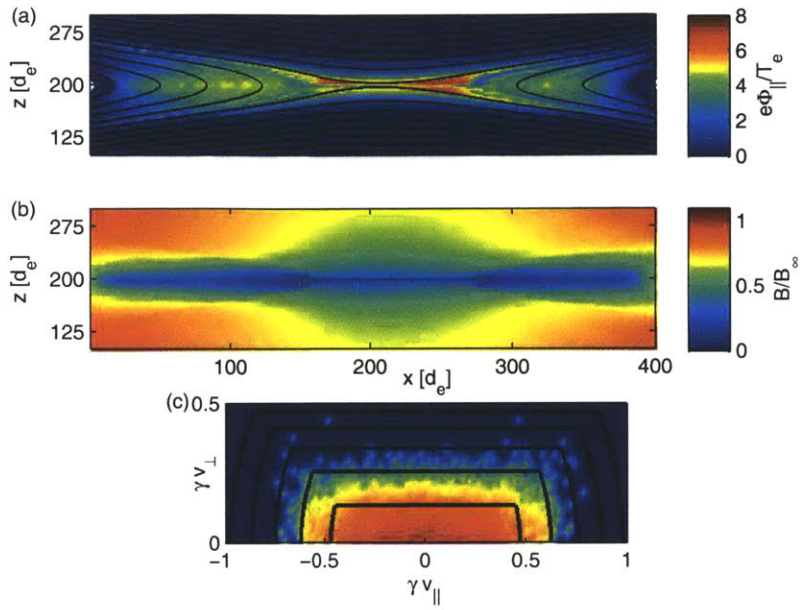

Figure 2-2: (colour) Comparison of electron distribution taken from a reconnection inflow in a kinetic simulation with Eq. (2.3). (a) Acceleration potential $e\Phi_{\parallel}/T_e$. (b) Magnetic field strength B/B_∞ (c) Particle data with contours of f superimposed, using $e\Phi_{\parallel}/T_e = 4.6$, $B/B_\infty = 0.3$.

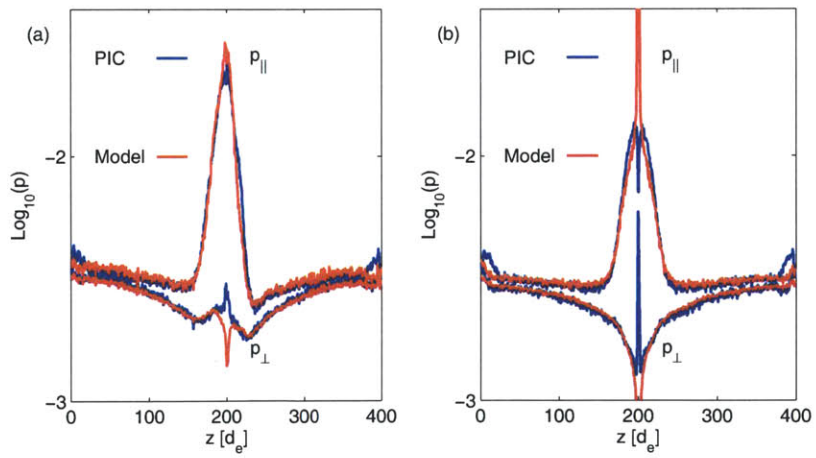

Figure 2-3: (colour) Comparison of the equations of state to data from kinetic simulations of (a) guide field reconnection with $B_g = 0.4B_0$ and (b) antiparallel reconnection.

momentum balance across the jets reveals that the plasma is marginally stable with respect to the electron firehose instability $B^2 = p_{\parallel} - p_{\perp}$, and it has been shown that the total current in the layer is insensitive to the reconnection electric field [33, 34]. The subsequent chapters will uncover the detailed structure of the electron diffusion region in antiparallel and small guide field reconnection, where the equations of state do not hold throughout the simulation domain.

Chapter 3

Structure of the electron diffusion region in antiparallel reconnection

The work in this chapter is largely based on the results of Ref. [34]

3.1 Orbit tracing

As shown in Chapter 2, the equations of state do not hold within the electron diffusion region in antiparallel reconnection due to the breakdown of the magnetic moment as an adiabatic invariant. Instead, f is determined numerically through the use of Liouville's theorem. Starting at a point within the diffusion region, the relativistic equations of motion for electrons with different initial velocities are integrated backwards in time using the electric and magnetic fields from a single time slice of the PIC simulation.

Once the electrons reach the region where the equations of state hold, the value of $f(\mathbf{x}, \mathbf{v})$ is obtained directly from Eq. (2.3) using the values of $\mathcal{E}$, μ and $\Phi_{\|}$ at a selected point on the particle trajectory within the inflow region.

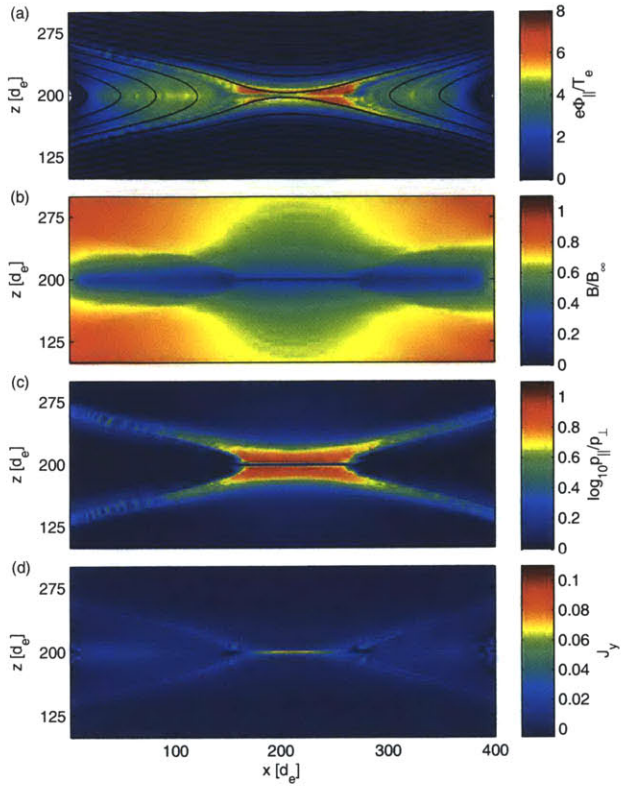

Figure 3-1: (colour) Time slice from an open-boundary PIC simulation of anti-parallel reconnection. (a) Acceleration potential $e\Phi_{\parallel}/T_e$. (b) Magnetic field strength B. (c) Pressure ratio $\log_{10}\left(p_{\parallel}/p_{\perp}\right)$. (d) Out of plane current density J_y.

3.2 Structure of the electron distribution

The orbit tracing method described above is applied to the results of simulations of antiparallel reconnection ($B_g = 0$) at mass ratio 400. The simulation domain is 2560×2560 cells $= 400d_e \times 400d_e$, where $d_e = c/\omega_{\rm pe}$ is the electron inertial skin depth. In Fig. 3-1, $\Phi_{\parallel}$, B, $\log_{10}(p_{\parallel}/p_{\perp})$ and J_y at time $t\Omega_{\rm ci} = 19$ are shown, after reconnection has become steady state. Close to the layer, $e\Phi_{\parallel}/T_e$ reaches a maximum value of approximately 7 while the ratio $p_{\parallel}/p_{\perp}$ is about 9.

The resulting distribution from a cut along the z-axis close to the x-line is shown in Fig. 3-2(a) where the coloured plots show the averaged values over v_x, v_y and v_z respectively. Within the layer, the distribution is highly structured, and a phase space hole in v_z [35] is observed, splitting the distribution into two somewhat triangular

portions which extend to large values of v_y. This hole is caused by the oscillatory electron motion (denoted meandering motion) in the diffusion region and the inversion layer of the in-plane electric field E_z [36]. Also observed are a number of striations, most noticeable in the v_x-v_y plane. Moving outside the layer, the separation in v_z and extension in v_y decrease, eventually becoming the elongated distribution characteristic of the inflow region.

Typical electron orbits in are shown in Fig. 3-2(b). On entering the layer, the electric and magnetic fields are well approximated by

$$\begin{aligned} \mathbf{E} &= E_y \hat{\mathbf{y}}, \\ \mathbf{B} &= B_0 (\frac{z}{d}\hat{\mathbf{x}} + \frac{x}{L}\hat{\mathbf{z}}). \end{aligned} \tag{3.1}$$

Here d and L are typical length scales, with $d \sim d_e$ and $L \gg d$. As such, the equations of motion can be written as

$$\begin{aligned} \ddot{x} &= -\frac{e}{m_e}\left(\dot{y} B_0 \frac{x}{L}\right) \\ \ddot{y} &= -\frac{e}{m_e}\left(E_y + \dot{z} B_0 \frac{z}{d} - \dot{x} B_0 \frac{x}{L}\right) \\ \ddot{z} &= -\frac{e}{m_e}\left(-\dot{y} B_0 \frac{z}{d}\right). \end{aligned} \tag{3.2}$$

If the E_y term in the y equation is assumed to dominate, the x and z equations of motion reduce to

$$\begin{aligned} \ddot{x} &= -\frac{e}{m_e}\left(\left(\dot{y}_0 - \frac{e}{m_e} E_y t\right) B_0 \frac{x}{L}\right) \\ \ddot{z} &= -\frac{e}{m_e}\left(-\left(\dot{y}_0 - \frac{e}{m_e} E_y t\right) B_0 \frac{z}{d}\right), \end{aligned} \tag{3.3}$$

whose solutions are linear combinations of Airy functions [3, 37]. This accounts for the oscillatory motion in the z direction and eventual ejection of the electrons in the x direction.

Taking moments of the reconstructed distribution, the density, fluid velocity and energy-momentum tensor can be calculated using numerical integration. Because of

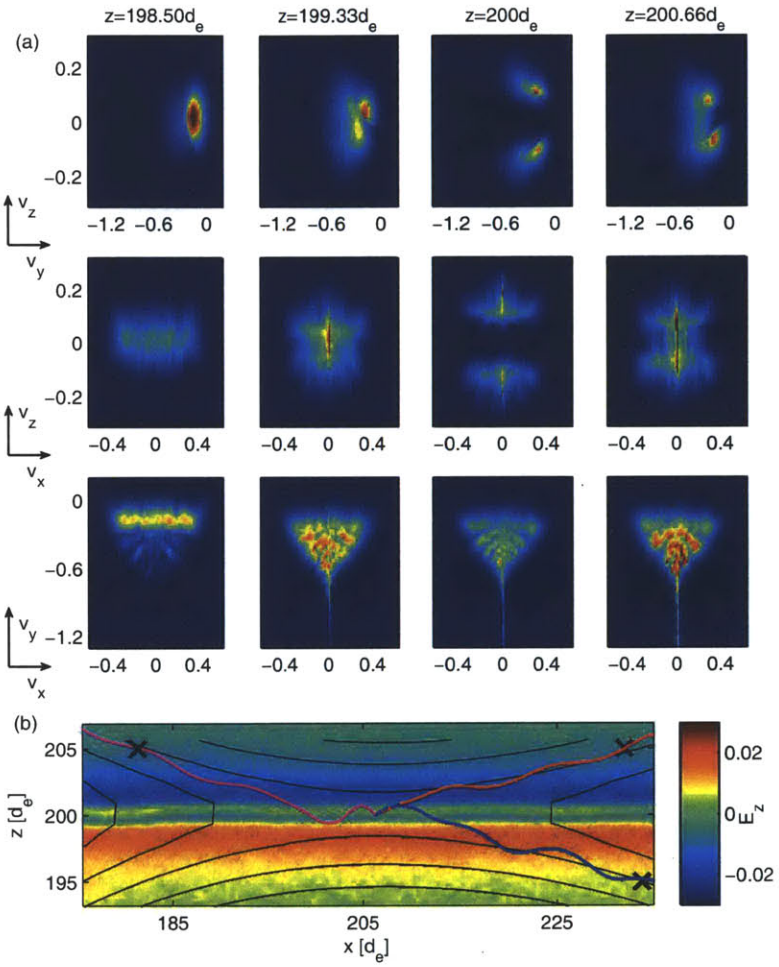

Figure 3-2: (colour) Plots of distribution function along a cut at $x = 206.25d_e$. Velocity units are in terms of c. (a) Distribution function averaged over γv_x, γv_y and γv_z where γ is the Lorentz factor. (b) Electron orbits from x-line with 0, 1 and 2 reflections. Colour plot is in-plane electric field E_z, with contours of in-plane projection of magnetic field lines.

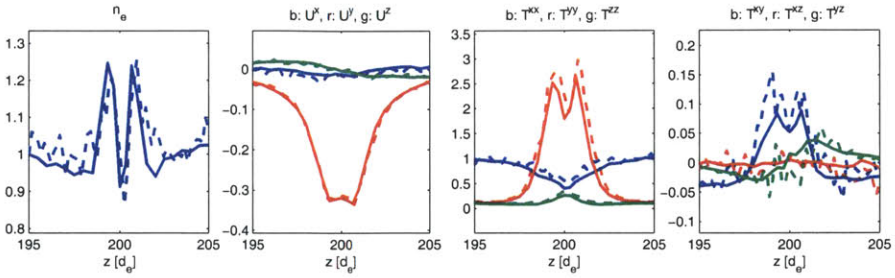

Figure 3-3: (colour) Moments of the electron distribution for a cut along the z axis passing through the x-line. From left to right, the density, fluid velocity, diagonal and off-diagonal components of the stress-energy tensor are plotted. The dashed lines show the data from the PIC simulation while the solid lines show the reconstructed moments. Density and stress-energy components are normalised to n_0 and T^{xx} outside the layer.

the presence of energetic electrons, the relativistic equations must be used, and the energy-momentum tensor is evaluated instead of the pressure tensor due to the nature of the data available (the pressure tensor is approximated by subtracting $n\langle U^i U^j\rangle$ from T^{ij}). From moments of the four-momentum $p^\mu = (E, \mathbf{p})$, the four flow, energy-momentum tensor and mean velocity are obtained as follows [38]

$$N^\mu = \int \frac{d^3p}{p^0} p^\mu f(x,p) \tag{3.4}$$

$$T^{\mu\nu} = \int \frac{d^3p}{p^0} p^\mu p^\nu f(x,p) \tag{3.5}$$

$$U^\mu = N^\mu / \sqrt{N^\nu N_\nu}. \tag{3.6}$$

In this simulation, the space-like components of N^μ are small and a good approximation for the fluid velocity. The validity of the reconstructed f is tested by comparing the moments with the data obtained directly from the PIC code. As shown in Fig. 3-3, good agreement is found between both sets of data. This provides evidence that the reconstructed distributions are accurate.

A more detailed three dimensional view of the reconstructed distribution function at locations around the x-line, is shown in Figs. 3-4(a)-(e). As mentioned earlier, the two main portions of the distribution ($v_z < 0$ and $v_z > 0$) are further divided by numerous striations. Tracing of orbits reveals that the regions between striations

are characterised by the number of times electrons are reflected in the z-direction within the layer before reaching the point of interest, with larger $|v_y|$ corresponding to a larger number of reflections. The trajectories shown in Fig. 3-2(b) have 0, 1 and 2 reflections. This classification due to the number of reflections has been seen in Refs. [39, 40], though they do not capture the full three dimensional structure of the electron distribution.

For comparison, particle data taken directly from the PIC simulation are presented in Figs. 3-4(f, g). This confirms the general form of the reconstructed distribution, and illustrates a key advantage of the orbit tracing method, in that the resolution achieved in both space and velocity space is much higher due to the ability to select as many velocity points as necessary (here 200^3 are used).

To explain the form of the individual regions it is important to note that just upstream of the layer $f(v_\parallel, v_\perp)$ is only large if $\frac{1}{2}mv_\perp^2 \leq T_e B/B_\infty$ and $\frac{1}{2}mv_\parallel^2 \leq e\Phi_\parallel$ where $T_e B/B_\infty \ll e\Phi_\parallel$. The centre of the various regions can thus be obtained by injecting electrons parallel to the outside magnetic field ($v_\perp = 0$), with $\frac{1}{2}mv_\parallel^2 \leq e\Phi_\parallel$. As the tip of each region consists of the highest energy electrons, their lengths are approximately determined by the acceleration potential $\Phi_\parallel$. The importance of $\Phi_\parallel$ is shown in Fig. 3-5, in which a reconstructed distribution function with $\Phi_\parallel = 0$ assumed in the inflow is compared to the distribution with the actual $\Phi_\parallel$ from the simulation. Without the large $\Phi_\parallel$ which gives rise to the elongated inflow distribution, the full length of the fingers in the reconstructed distribution is not observed.

The different parts of the distribution correspond to electrons originating from the four quadrants in the x-z plane. By considering their trajectories, it is clear that those with positive v_x originated from the left of the x-line, and those with negative v_x from the right. The entry z position is determined by the number of reflections and the sign of v_z. For example, the trajectory with two reflections in Fig. 3-2(b) contributes to the third "finger" in the bottom-right of the distribution.

The entry angle $\angle(v_y, v_x)$ of the parallel streaming electrons is similar to $\angle(B_y, B_x)$ at the entry position. This entry angle and the $v_x B_z$ magnetic forces, which help turn parts of the entry v_x into the y-direction, control the angle between the striations of f

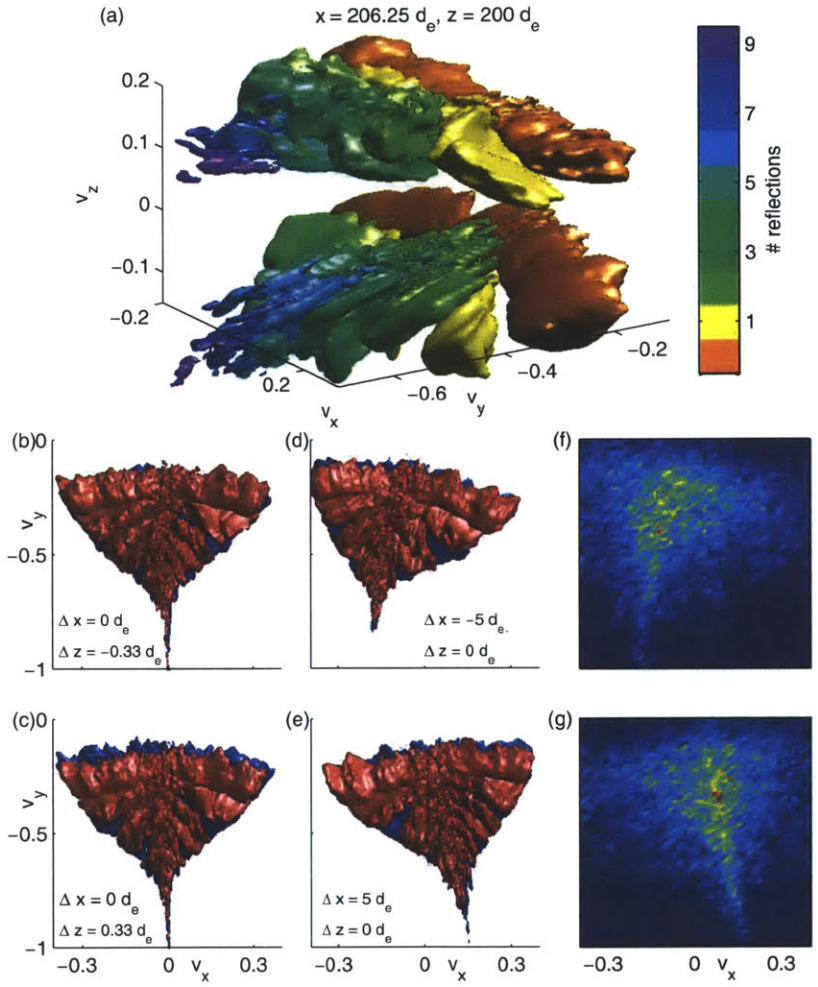

Figure 3-4: (colour) Electron distribution within neutral sheet. (a) Isosurface of the distribution at x-line. The different colours correspond to the number of times the electrons are reflected in the layer. (b), (c) Isosurfaces of the distribution at $\Delta z = \pm 0.33 d_e$ above and below x-line at $(x, z) = (206.25, 200)$. The red region lies in $v_z > 0$, the blue in $v_z < 0$. Note the relative displacement in v_y of the red and blue surfaces as z increases, causing a gradient in P_{yz}. (d), (e) Isosurfaces of the distribution at $\Delta x = \pm 5 d_e$ to the left and right of the x-line. Rotation of the distribution along the layer causes the gradient in P_{xy}. (f), (g) v_x-v_y distribution of particles taken from PIC simulation at $\Delta x = \pm 5 d_e$.

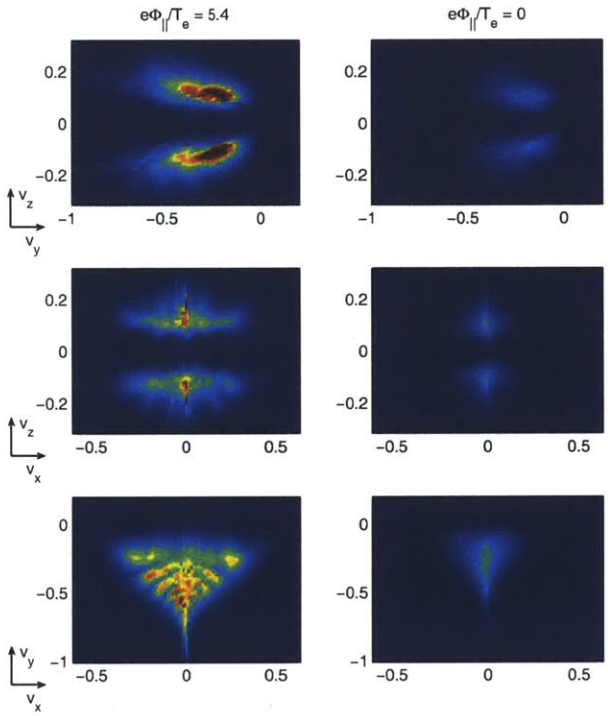

Figure 3-5: (colour) Comparison of the reconstructed distribution using $e\Phi_{\|}/T_e = 5.4$ (from simulation data) and 0 (assuming only magnetic trapping). The importance of the parallel potential in determining the length of the fingers is evident.

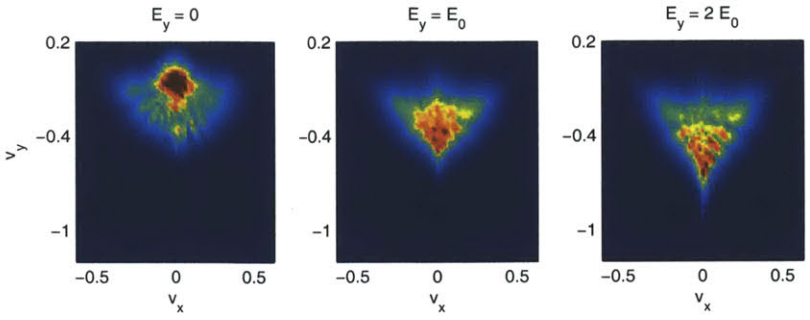

Figure 3-6: (colour) Electron distributions averaged over v_z at the x-line from simulations in which the force of E_y on the electrons is modified. In the left plot, there is no elongation due to the absence of E_y. The centre plot shows the distribution in the unmodified simulation, while there is increased electron acceleration in the final plot, where E_y has been effectively doubled.

in the v_x-v_y plane and varies discretely with the number of reflections. From here, it can be seen how the inflow anisotropy drives the current, as the large parallel steaming velocity of the electrons upstream of the layer gets turned into the y-direction by the entry angle and by the magnetic forces. Finally, the narrow "tip" of the distribution with high number of reflections is due to the longer time this limited class of electrons are accelerated by E_y.

The role of E_y in the acceleration of electrons in the narrow tip can be shown numerically. A series of simulations with parameters described in [34] was performed, in which an additional force was applied to electrons in a $40d_e \times 3d_e$ box around the x-line. In one simulation, this external force cancelled the E_y component of the Lorentz force, while in another, the additional force doubled E_y. At all times were Maxwell's equations solved self-consistently. The electron distributions at the x-line from these simulations are shown in Fig. 3-6, and the dependence of the length of the tip on E_y is clear. In all cases, there is still turning of the electron velocity in the y direction due to the effects of the magnetic field.

Finally, the structure of the distribution also accounts for the momentum balance in the direction of the reconnection electric field. Close to the x-line, B vanishes and

the off-diagonal terms of the pressure tensor are dominant, balancing the electric field

$$E_y \simeq -\frac{1}{ne}\left(\nabla \cdot \mathbf{P}\right)_y = -\frac{1}{ne}\left(\frac{\partial P_{xy}}{\partial x} + \frac{\partial P_{yz}}{\partial z}\right) \tag{3.7}$$

where the frozen in condition $\mathbf{E}+\mathbf{v}\times\mathbf{B} = 0$ is broken by electron meandering motion [41]. These terms arise from the small changes in the distribution function between different positions. In Figs. 3-4(b, c) (and Fig. 3-2(a)), moving from below to above x-line, we observe that the $v_z < 0$ portion of the distribution begins slightly displaced in the negative v_y direction relative to the $v_z > 0$ portion and ends slightly displaced in the positive v_y direction, giving rise to a gradient in P_{yz}. The displacements are due to the different times electrons spend in the diffusion region, which affects the change in v_y due to acceleration by the reconnection electric field. The gradient in the P_{xy} term arises from the rotation of the distribution in the v_x-v_y plane as one moves along x, which is shown in Figs. 3-4(d, e).

To summarize, the inflow electron pressure anisotropy is responsible for the structure of the electron diffusion region in anti-parallel reconnection. The incoming electrons into the layer stream along field lines with little perpendicular velocity. Their entry location determines their initial velocity in the out-of-plane y-direction and depending on the number of bounces in the layer, v_y is further increased by magnetic force turning part of the initial v_x into the y-direction. This yields highly structured and striated electron distributions uncovered here for the first time. The reconnection electric field, E_y is responsible for more subtle structures in f, important for momentum balance at the x-line.

Chapter 4

Structure of the electron diffusion region in small guide field reconnection

Reconnection events with an out of plane magnetic component are more likely to be observed [42, 43], and the addition of a guide field to the antiparallel reconnection geometry can change the structure of the reconnection region dramatically. While at mass ratio 400, the electron jets described in Chapter 2 are observed up to guide fields of $B_g = 0.14B_0$, recent full mass ratio simulations have shown that the jets no longer exist even for extremely small guide fields ($B_g \gtrsim 0.05B_0$) [42]. The effects of small guide fields on experimental observations of reconnection will thus play an important role, and it is necessary to understand how the structure of the diffusion region changes with B_g.

In this chapter results from mass ratio 400 simulations are first presented to illustrate the changes in the distribution function as the guide field is gradually increased from $0.05B_0$ to $0.2B_0$. The results of full mass ratio simulations, where the transition is sharper, will then be shown.

4.1 Mass ratio 400 simulations

The simulations used have the same parameters as described in Section 3.2, with the value of B_g being the only variable changed between simulations. Again, the orbit tracing method is applied to fields from time slices after reconnection has become steady state, and the form of the distribution function is thereby obtained. In Fig. 4-1 plots of B_y and E_z in simulations with different values of B_g are shown. The leftmost column shows the effect of the guide field on the quadrupolar Hall magnetic fields – B_g adds to the fields in the top-right and bottom-left regions, and opposes the fields in the top-left and bottom right, breaking the symmetry of the system. The second and third columns show the existence of the elongated region for guide fields up to $B_g = 0.14B_0$, and the disappearance of the jets at $B_g = 0.2B_0$.

A comparison between the x-line distributions for $B_g = 0$ and $B_g = 0.05B_0$ is shown in Fig. 4-2. While the two distributions are similar, there are clear differences between their structures. In the top panels (v_y-v_z plane), the phase space hole in v_z closes as B_g is increased, and f is large around a region with small v_z,v_x and negative v_y. Protruding from this central regions are a number of "fingers" with different inclinations, which are most easily seen in the v_x-v_z plane.

The lack of a phase space hole in v_z is most easily explained and is due to the lack of the inversion layer of the in plane electric field E_z in the diffusion region [36], which allows electrons with small v_z to reach the x-line. In order to understand the other features of the distribution, it is once again useful to trace the origin of the particles from different regions, and count the number of times they cross $z = 200d_e$. This is illustrated in the three dimensional plot of the distribution and some characteristic orbits shown in Fig. 4-3.

The electrons in regions with large f correspond to two types of trajectories. In the central region, orbits are similar to those shown in Fig. 4-3(b), coming from the top right and bottom left quadrants in the inflow, where the guide field is in the same direction as the quadrupolar Hall field. Within the fingers, the orbits are like those in Fig. 4-3(c), coming from the regions where the guide field is in the opposite direction

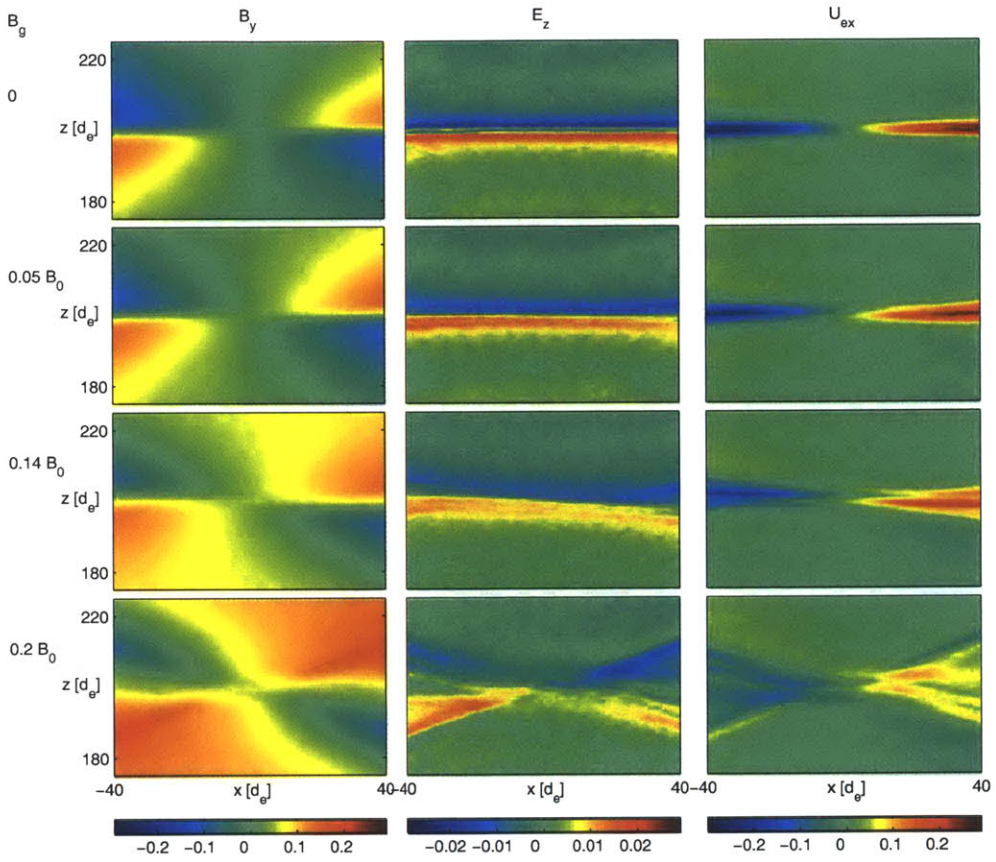

Figure 4-1: (colour) Changes in the reconnection geometry as the guide field is increased from 0 to $0.2B_0$. The leftmost column shows the out-of-plane magnetic field B_y, the middle column shows the in-plane electric field E_z and the rightmost column shows the electron flow velocity U_{ex}.

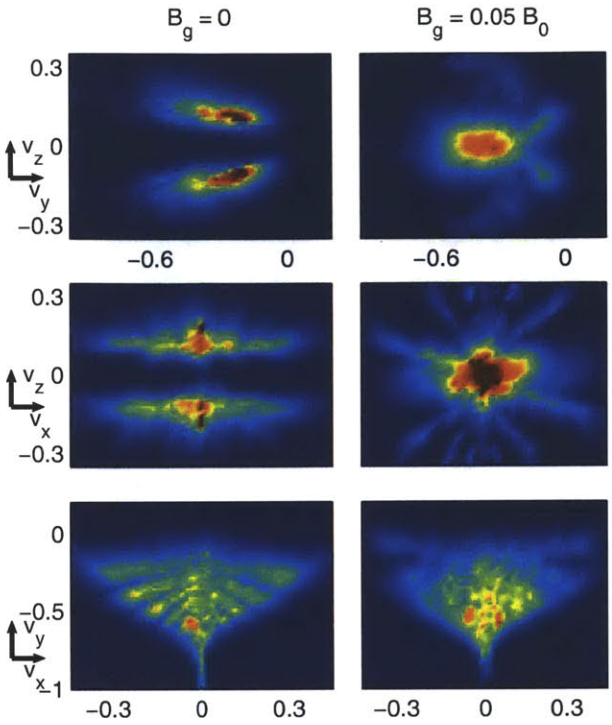

Figure 4-2: (colour) Electron distributions at the x-line for antiparallel (left) and $B_g = 0.05B_0$ guide field (right) reconnection.

to the quadrupole field. On entering the layer, the particles exhibit oscillatory z motion with a large amplitude as they are ejected in the x direction. The nature of these orbits also explains the alternation of the sign of v_z with the number of reflections for electrons with the same v_x sign. As the electrons in the fingers come from a lower B region with a thinner distribution (in the $v_\perp$ direction), the fingers are thinner than the central region. This behaviour is unlike the antiparallel case, where all particles undergo similar types of motion.

The motion of electrons in the central area is well approximated by the model in Ref. [42], in which the equations of motion Eq. (3.3) are modified by the addition of the guide field and the replacement of the expression for v_y with the mean y fluid velocity. Setting $e/m_e = 1$ for convenience,

$$\begin{aligned} \ddot{x} &= -\langle U_y \rangle B_0 \frac{x}{L} + \dot{z} B_y \\ \ddot{z} &= \langle U_y \rangle B_0 \frac{z}{d} - \dot{x} B_y, \end{aligned} \tag{4.1}$$

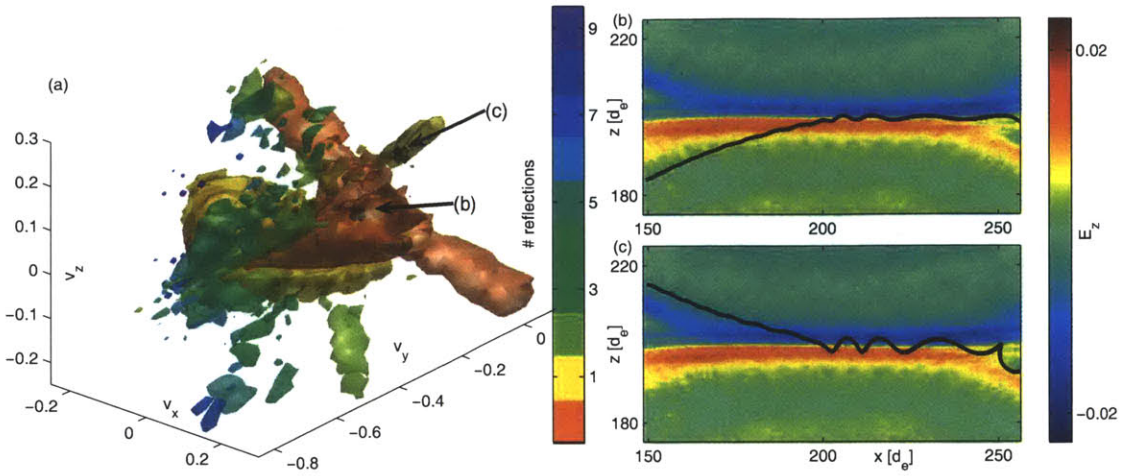

Figure 4-3: (colour) (a) Isosurfaces of the electron distribution at the x-line for $B_g = 0.05B_0$. Colours show the number of times an electron is reflected before reaching the x-line. (b) Trajectory of an electron from the point marked (b) in velocity space. (c) Trajectory of electron from point (c).

The resulting linear equations of motion then account for vertical deflection of the trajectories as the electrons are ejected from the layer.

A slight modification of the approximation is also useful in understanding the motion of particles in the fingers. Replacement of the fluid velocity by the mean v_y in the fingers provides a qualitative description of their motion, and provides additional information on some of the features of the distribution.

As seen in Figs. 4-2 and 4-3(a), the fingers in the distribution are inclined in both the v_x-v_y and v_x-v_z planes. The inclination in the v_x-v_y plane of the fingers with no reflections is due to the field-aligned motion in the inflow – the addition of the guide field means that the direction of the magnetic field just outside the layer is no longer purely in the x direction as in the antiparallel case. As in the antiparallel case, the large $\Phi_{||}$ outside the layer determines the length of the fingers. The presence of the guide field ($B_y > 0$ near the x-line) also causes acceleration in the z direction due to the $v_x B_y$ force, which accounts for the initial inclination in the v_x-v_z plane.

As the number of reflections increases, the angle of inclination (measured from the v_x axis) increases and the mean v_y increases. The increase in $|v_y|$ is due to acceleration by the reconnection electric field. The decrease in $|v_x|$ also follows from Eq. (4.1). The

$v_z B_y$ term is small when averaged over an oscillation period, so particles travelling towards the x-line are decelerated in a similar manner to the antiparallel case. A complete explanation of the acceleration in z requires the use of the full equation of motion and must be solved numerically.

Figure 4-4 provides an illustration of how the fingers from different positions in the diffusion region are related. In Fig. 4-4(a) and (b) distributions from the x-line and a point $5d_e$ to its left are displayed. The three coloured points in each figure correspond to electrons following the trajectories in Fig. 4-4(c), and the point at which the distribution in (a) is evaluated is the average position of where the three trajectories first cross $z = 200d_e$. As the electrons move from (a), where they lie in the finger with no reflections, to (b), their positions in velocity space evolve until they eventually reside in the finger with one reflection in the distribution at the x-line. These numerical results thus demonstrate how the fingers in the distribution are related to one another.

As the guide field is increased, the distribution function is modified. This progression is displayed in Fig. 4-5. The structure of the central region remains the same, and the changes are mostly seen in the fingers. Most evidently, in the v_x-v_y plane, they increase in inclination as B_g increases, due to the orientation of the external magnetic field as mentioned earlier. The difference between the $B_g = 0.2B_0$ case and the other distributions is due to the different field geometry, as the elongated electron layer is no longer present. Nevertheless, the general structure of the distribution at the x-line is similar. Thus, as B_g increases with the field geometry remaining similar, the effects on the distribution are small.

4.2 Mass ratio 1836 simulations

In the full mass ratio simulations, the size of the simulation domain in terms of d_i is maintained, and is 5120×5120 cells $= 857d_e \times 857d_e$. All other parameters remain as described in Section 3.2. In agreement with [42], the electron jets are not present even at the lowest guide field $B_g = 0.05B_0$, though there is a somewhat elongated

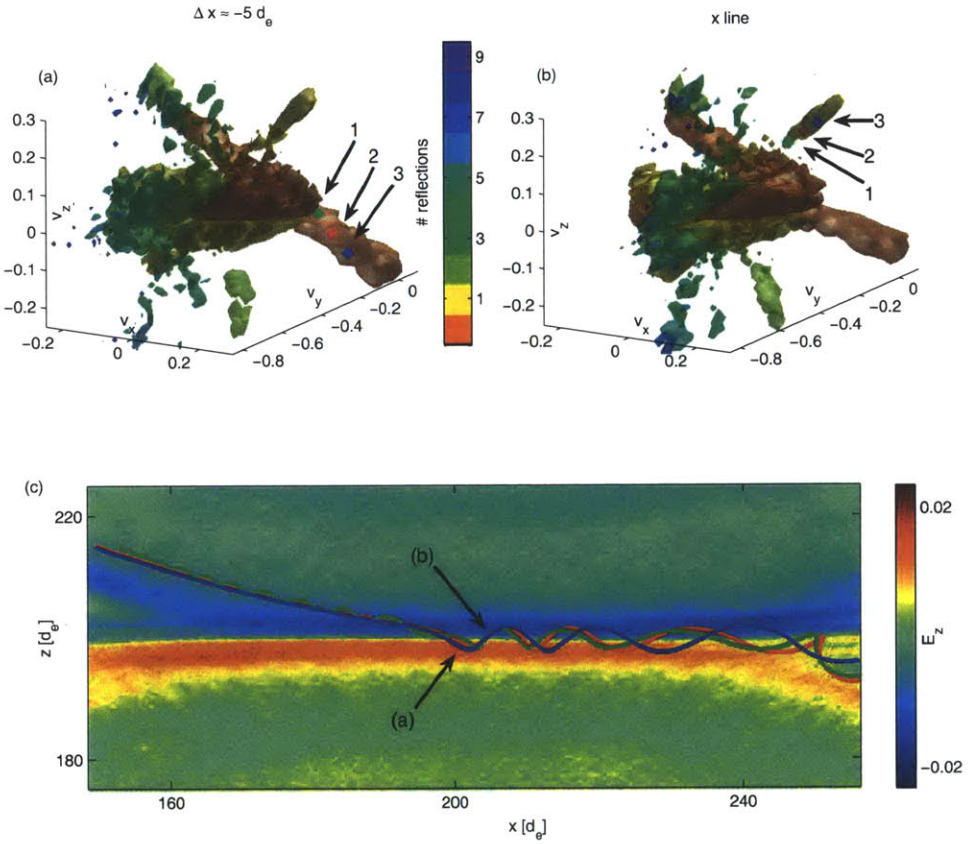

Figure 4-4: (colour) A demonstration of the evolution of the velocity space positions of electrons in the fingers. Electrons from the zero-reflection finger in (a) follow the trajectories in (c) until they reach the one-reflection finger at the x-line (b). The distribution in (a) is taken from the average x position of the $z = 200d_e$ crossings of the three trajectories.

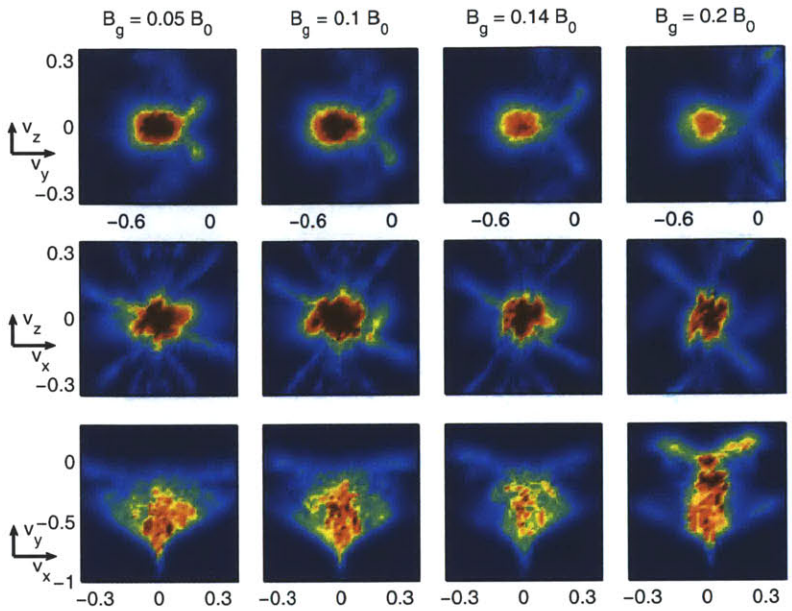

Figure 4-5: (colour) Electron distributions at the x-line from simulations of reconnection with increasing guide fields. From left to right, $B_g = 0.05B_0$, $0.1B_0$, $0.14B_0$ and $0.2B_0$. At the largest guide field, the elongated electron jet is no longer present and the field structure is different.

diffusion region. As such, the distribution at this B_g would be expected to be similar to the $B_g = 0.14B_0$ and $B_g = 0.2B_0$ distributions at mass ratio 400, while those at slightly larger B_g would be similar to the $B_g = 0.2$ case at mass ratio 400.

Reconstructed distribution functions from the full mass ratio simulations are presented in Fig. 4-6. In the antiparallel case, the distribution largely resembles the distribution in the mass ratio 400 simulation shown in Fig. 3-4. At $B_g = 0.05B_0$, which is close to the transition between reconnection regions with and without the electron jets, the distribution has similarities to both the $B_g = 0.14B_0$ and $0.2B_0$ distributions at mass ratio 400. As B_g is increased to $0.1B_0$, where there are no jets and the exhaust is not magnetised, the distribution becomes more like the $B_g = 0.2B_0$ case in the lower mass ratio simulation. At guide fields above $B_g = 0.14B_0$, the exhaust becomes magnetised and the equations of state hold throughout the simulation domain.

The results of these simulations have shown that the addition of a small guide field at realistic mass ratios leads to a dramatic modification of the reconnection

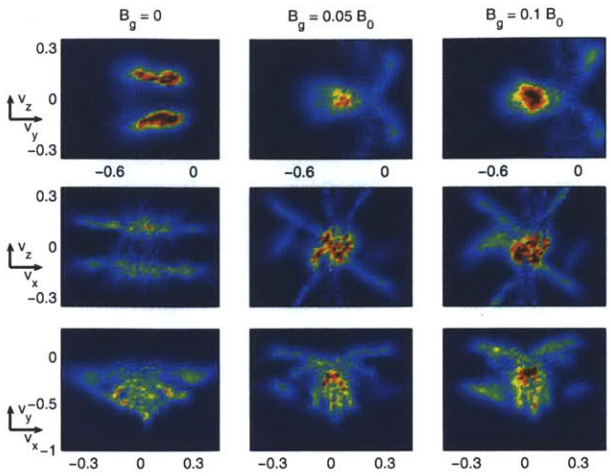

Figure 4-6: (colour) Electron distributions at the x-line from full mass ratio simulations. From left to right, the $B_g = 0$ (antiparallel), $0.05B_0$ and $0.1B_0$. The antiparallel case is very similar to the mass ratio 400 antiparallel simulation, while the $B_g \neq 0$ cases are similar to larger guide field simulations at mass ratio 400.

geometry and the distribution function. As reconnection in the magnetotail takes place with guide fields in different regimes [15, 16, 27], these results are relevant to NASA's upcoming MMS mission [21], which will be able to resolve the electron diffusion region and electron distributions. In addition, the results also emphasise the importance of the mass ratio in simulations of reconnection.

Chapter 5

Conclusion

The electron diffusion region in collisionless reconnection has been studied using orbit tracing techniques on data from kinetic simulations of magnetic reconnection. In antiparallel reconnection, it has been shown that the strong inflow electron pressure anisotropy is responsible for the highly structured nature of the electron distribution in this region, and the origin of the off-diagonal terms of the pressure tensor has been revealed.

In the case of reconnection with a small guide field, the structure of the distribution is different from the antiparallel case, and these differences can be explained by considering the motion of single particles in the fields. It has also been shown that the reconnection geometry is sensitive to the mass ratio when guide fields are present, and this raises questions about the applicability of the results of low mass ratio simulations to spacecraft data with similar guide fields.

These results will be particularly relevant to the Magnetospheric-Multiscale (MMS) mission, which is projected for launch in 2014. The spacecraft will have particle detectors with extremely high time resolution, allowing it to resolve the three dimensional structure of the electron distribution in the diffusion region, which has been studied in this thesis.

Bibliography

[1] F. F. Chen. Introduction to plasma physics and controlled fusion. Plenum Press, New York, 1984.

[2] J. Freidberg. Plasma Physics and Fusion Energy. Cambridge University Press, 2007.

[3] E. Priest and T. Forbes. Magnetic Reconnection. Cambridge University Press, 2000.

[4] Masaaki Yamada, Russell Kulsrud, and Hantao Ji. Magnetic reconnection. Rev. Mod. Phys., 82:603–664, Mar 2010.

[5] Masaaki Yamada. Understanding the dynamics of magnetic reconnection layer. Space Science Reviews, 160:25–43, 2011. 10.1007/s11214-011-9789-5.

[6] S. von Goeler, W. Stodiek, and N. Sauthoff. Studies of internal disruptions and m=1 oscillations in tokamak discharges with soft X-ray techniques. Phys. Rev. Lett., 33(20):1201–1203, NOV 1974.

[7] J.W. Dungey. Lxxvi. conditions for the occurrence of electrical discharges in astrophysical systems. Philosophical Magazine Series 7, 44(354):725–738, 1953.

[8] E. N. Parker. Sweet's mechanism for merging magnetic fields in conducting fluids. J. Geophys. Res., 62:509–520, DEC 1957.

[9] J. F. Drake, M. A. Shay, and M. Swisdak. The hall fields and fast magnetic reconnection. Physics of Plasmas, 15(4):042306, 2008.

[10] B. N. Rogers, R. E. Denton, J. F. Drake, and M. A. Shay. Role of dispersive waves in collisionless magnetic reconnection. Phys. Rev. Lett., 8719(19):195004, NOV 5 2001.

[11] William Daughton, Jack Scudder, and Homa Karimabadi. Fully kinetic simulations of undriven magnetic reconnection with open boundary conditions. Physics of Plasmas, 13(7):072101, 2006.

[12] Hantao Ji, Masaaki Yamada, Scott Hsu, and Russell Kulsrud. Experimental test of the sweet-parker model of magnetic reconnection. Phys. Rev. Lett., 80:3256–3259, Apr 1998.

[13] H. E. Petschek. Magnetic Field Annihilation. NASA Special Publication, 50:425, 1964.

[14] J. Birn, J. F. Drake, M. A. Shay, B. N. Rogers, R. E. Denton, M. Hesse, M. Kuznetsova, Z. W. Ma, A. Bhattacharjee, A. Otto, and P. L. Pritchett. Geospace environmental modeling (GEM) magnetic reconnection challenge. J. Geophys. Res., 106(A3):3715–3719, MAR 1 2001.

[15] M. Oieroset, T. Phan, M. Fujimoto, R. P. Lin, and R. P. Lepping. In situ detection of collisionless reconnection in the Earth's magnetotail. Nature, 412(6845):414–417, JUL 26 2001.

[16] T. D. Phan, J. F. Drake, M. A. Shay, F. S. Mozer, and J. P. Eastwood. Evidence for an elongated (> 60 ion skin depths) electron diffusion region during fast magnetic reconnection. Phys. Rev. Lett., 99(25), DEC 21 2007.

[17] Yang Ren, Masaaki Yamada, Stefan Gerhardt, Hantao Ji, Russell Kulsrud, and Aleksey Kuritsyn. Experimental verification of the hall effect during magnetic reconnection in a laboratory plasma. Phys. Rev. Lett., 95:055003, Jul 2005.

[18] V. M. Vasyliunas. Theoretical models of magnetic field line merging. Reviews of Geophysics, 13(1):303–336, FEB 1975.

[19] Carolus J. Schrijver and George L. Siscoe, editors. Heliophysics: Plasma Physics of the Local Cosmos. Cambridge University Press, 2009.

[20] M. Øieroset, T. D. Phan, J. P. Eastwood, M. Fujimoto, W. Daughton, M. A. Shay, V. Angelopoulos, F. S. Mozer, J. P. McFadden, D. E. Larson, and K.-H. Glassmeier. Direct evidence for a three-dimensional magnetic flux rope flanked by two active magnetic reconnection x lines at earth's magnetopause. Phys. Rev. Lett., 107:165007, Oct 2011.

[21] A. Surjalal Sharma and Steven A. Curtis. Magnetospheric multiscale mission. In W.B. Burton, J. M. E. Kuijpers, E. P. J. Heuvel, H. Laan, I. Appenzeller, J. N. Bahcall, F. Bertola, J. P. Cassinelli, C. J. Cesarsky, O. Engvold, R. McCray, P. G. Murdin, F. Pacini, V. Radhakrishnan, K. Sato, F. H. Shu, B. V. Somov, R. A. Sunyaev, Y. Tanaka, S. Tremaine, N. O. Weiss, A. Surjalal Sharma, and Predhiman K. Kaw, editors, Nonequilibrium Phenomena in Plasmas, volume 321 of Astrophysics and Space Science Library, pages 179–195. Springer Netherlands, 2005. 10.1007/1-4020-3109-2_8.

[22] A. Le, J. Egedal, W. Daughton, W. Fox, and N. Katz. Equations of state for collisionless guide-field reconnection. Phys. Rev. Lett., 102(8):085001, FEB 27 2009.

[23] Philip Pritchett. Particle-in-cell simulation of plasmas- a tutorial. In Jörg Büchner, Manfred Scholer, and Christian Dum, editors, Space Plasma Simulation, volume 615 of Lecture Notes in Physics, pages 1–24. Springer Berlin / Heidelberg, 2003. 10.1007/3-540-36530-3_1.

[24] Paolo Ricci, J. U. Brackbill, W. Daughton, and Giovanni Lapenta. Collisionless magnetic reconnection in the presence of a guide field. Physics of Plasmas, 11(8):4102–4114, 2004.

[25] K. J. Bowers, B. J. Albright, L. Yin, B. Bergen, and T. J. T. Kwan. Ultrahigh performance three-dimensional electromagnetic relativistic kinetic plasma simulation. Physics of Plasmas, 15(5):055703, 2008.

[26] E. Harris. On a plasma sheath separating regions of oppositely directed magnetic field. Il Nuovo Cimento (1955-1965), 23:115–121, 1962. 10.1007/BF02733547.

[27] L. J. Chen, N. Bessho, B. Lefebvre, H. Vaith, A. Fazakerley, A. Bhattacharjee, P. A. Puhl-Quinn, A. Runov, Y. Khotyaintsev, A. Vaivads, E. Georgescu, and R. Torbert. Evidence of an extended electron current sheet and its neighboring magnetic island during magnetotail reconnection. J. Geophys. Res., 113(A12), DEC 19 2008.

[28] M. Oieroset, R. Lin, and T. Phan. Evidence for electron acceleration up to 300 keV in the magnetic reconnection diffusion region of earth's magnetotail. Phys. Rev. Lett., 89(19):195001, NOV 4 2002.

[29] J. Egedal, M. Øieroset, W. Fox, and R. P. Lin. *In Situ* discovery of an electrostatic potential, trapping electrons and mediating fast reconnection in the earth's magnetotail. Phys. Rev. Lett., 94:025006, Jan 2005.

[30] J. Egedal, W. Fox, N. Katz, M. Porkolab, M. Oieroset, R. P. Lin, W. Daughton, and Drake J. F. Evidence and theory for trapped electrons in guide field magnetotail reconnection. J. Geophys. Res., 113(6):A12207, MAR 25 2008.

[31] J. Egedal, A. Le, P. L. Pritchett, and W. Daughton. Electron dynamics in two-dimensional asymmetric anti-parallel reconnection. Physics of Plasmas, 18(10):102901, 2011.

[32] J. Egedal, W. Daughton, J. F. Drake, N. Katz, and A. Le. Formation of a localized acceleration potential during magnetic reconnection with a guide field. Phys. Plasmas, 16(5):050701, MAY 2009.

[33] A. Le, J. Egedal, W. Fox, N. Katz, A. Vrublevskis, W. Daughton, and J. F. Drake. Equations of state in collisionless magnetic reconnection. Phys. Plasmas, 17(5):055703, MAY 2010. 51st Annual Meeting of the Division of Plasma Physics of the American Physical Society, Atlanta, GA, NOV 02-06, 2009.

[34] J. Ng, J. Egedal, A. Le, W. Daughton, and L.-J. Chen. Kinetic structure of the electron diffusion region in antiparallel magnetic reconnection. Phys. Rev. Lett., 106:065002, Feb 2011.

[35] R. Horiuchi and H. Ohtani. Formation of non-maxwellian distribution and its role in collisionless driven reconnection. Commun. Comput. Phys, 4(3):496–505, 2008.

[36] Li-Jen Chen, William S. Daughton, Bertrand Lefebvre, and Roy B. Torbert. The inversion layer of electric fields and electron phase-space-hole structure during two-dimensional collisionless magnetic reconnection. Physics of Plasmas, 18(1):012904, 2011.

[37] T.W. Speiser. Conductivity without collisions or noise. Planetary and Space Science, 18(4):613 – 622, 1970.

[38] S. R. de Groot, W. A. van Leeuwen, and Ch. G. van Weert. Relativistic Kinetic Theory. North-Holland Publishing Company, 1980.

[39] A. Divin, S. Markidis, G. Lapenta, V. S. Semenov, N. V. Erkaev, and H. K. Biernat. Model of electron pressure anisotropy in the electron diffusion region of collisionless magnetic reconnection. Physics of Plasmas, 17(12):122102, 2010.

[40] Keizo Fujimoto and Richard D. Sydora. Particle description of the electron diffusion region in collisionless magnetic reconnection. Physics of Plasmas, 16(11):112309, 2009.

[41] A. Ishizawa, R. Horiuchi, and H. Ohtani. Two-scale structure of the current layer controlled by meandering motion during steady-state collisionless driven reconnection. Physics of Plasmas, 11(7):3579–3585, 2004.

[42] M. V. Goldman, G. Lapenta, D. L. Newman, S. Markidis, and H. Che. Jet deflection by very weak guide fields during magnetic reconnection. Phys. Rev. Lett., 107:135001, Sep 2011.

[43] M. Swisdak, J. F. Drake, M. A. Shay, and J. G. McIlhargey. Transition from antiparallel to component magnetic reconnection. J. Geophys. Res, 110(A5):A05210, 2005.